LARGE-SCALE NUMERICAL ANALYSIS OF MULTI-PASS WELDING USING AUTOMESH AND IDEALIZED EXPLICIT FEM

W. WANG*, S. SASAKI*, S. MAEDA*, K. IKUSHIMA*, M. SHIBAHARA*

**Graduate school of engineering, Osaka Metropolitan University, Japan*

DOI 10.3217/978-3-99161-089-2-037, license CC BY 4.0

ABSTRACT

This study introduces a numerical framework that combines the highly efficient automatic mesh generation system, Automesh, with the Idealised Explicit Finite-Element Method (IEFEM) to enable large-scale thermo-elastic–plastic analyses of multi-pass welding. Automesh converts engineering parameters into graded, analysis-ready meshes while enforcing equal unit heat-input density per pass and consistent element quality and pass placement across cases, thereby ensuring fair comparisons. IEFEM employs a dynamic-explicit formulation with local (node/element-level) updates, substantially reducing memory usage and runtime and admitting efficient GPU parallelisation. Two parametric campaigns on X-groove and V-groove joints deliver pass-resolved, time-accurate fields of temperature, stress, and strain. Within the investigated ranges, groove depths near half the plate thickness minimised deformation; decreasing groove angle reduced accumulated lineal heat input and thus deformation; and root gap showed little effect for $g = 1 \sim 10$ mm. Discrete jumps in angular distortion were traced to changes in the number of passes within a dominant height band, which placed sub-passes near the peak of an empirical $Q/h_{\max}^2$ response. Automesh reduced meshing from hours to under 10 seconds per case, and IEFEM cut solution time by roughly an order of magnitude versus representative implicit baselines, yielding an efficient and reliable workflow for industrial studies and database construction.

Keywords: large-scale welding simulation; idealized explicit finite element method; automatic mesh generation; thermo-elastic-plastic analysis; multi-pass weld joints; transverse shrinkage; angular distortion

INTRODUCTION

Welding is indispensable for the fabrication of a wide range of industrial products and large-scale structures. However, a highly concentrated moving heat flux causes severe thermal and mechanical loading in thick plates and massive components of multi-pass welding. After completion of the weld, substantial residual stresses and geometric distortions may

accumulate, jeopardising structural integrity and dimensional accuracy [1]. To optimise the manufacturing route and guarantee product quality, it is essential to predict the transient temperature field produced by the moving heat source together with the stress and displacement fields it induces [2]. Conventional thermo-elastic-plastic analyses based on static implicit finite-element methods encounter significant challenges in this task because strongly nonlinear molten regions travel through space and time, forcing extremely fine meshes and iterative solvers that inflate run-time and memory demand [3].

To overcome these limitations, we have developed the Idealised Explicit Finite-Element Method (IEFEM) [4]. IEFEM is rooted in a dynamic explicit FEM framework [5] but is specialised for transient welding phenomena. By adopting an explicit time-integration scheme and confining calculations to element- and node-local operations, IEFEM eliminates the global iterative solvers required by implicit schemes while preserving accuracy virtually equivalent to the static implicit formulation. The local-operation architecture dramatically suppresses memory usage and accelerates computation. Moreover, it is well-suited to massive parallelisation on graphics processing units (GPUs). With recent advances in GPU hardware and parallel algorithms [6-8], three-dimensional moving heat-source analyses of multi-pass weld joints - long deemed infeasible - can now be executed relatively easily [9]. Thus, IEFEM constitutes one of the two central numerical pillars that enable the ultra-large-scale simulations presented in this study.

Mesh generation represents a second bottleneck. Generic mesh generators such as Triangle [10], TetGen [11], Gmsh [12], and the CGAL library [13] have progressed from two-dimensional to fully automatic three-dimensional meshing and now integrate CAD interfaces with post-processing capabilities; nevertheless, accurately treating weld-specific complexities - root geometry, reinforcement, and the heat-affected zone (HAZ) - still demands bespoke scripts and meticulous parameter tuning. Early welding-oriented studies, exemplified by Lindgren's classical thermo-mechanical analyses [14], the theoretical framework of Goldak and Akhlaghi [1], and the multi-pass pipe simulation by Ikushima and Shibahara [15], likewise relied on expert-guided model construction and mesh adaptation, limiting their scalability to large industrial problems. More recently, adaptive subdivision techniques - such as the selective-integration adaptive mesh refinement proposed by Huang and Murakawa [16] and the octree-based scheme of Chen *et al.* [17] - have been introduced. Yet, their configuration remains intricate, and they have not achieved widespread generalisation. Industry practitioners, therefore, continue to emphasise the inherent limits on reproducibility and lead time imposed by manual modelling workflows [18].

In this study, we have developed Automesh, an automated meshing system that parameterises variables such as the bead width, groove angle, reinforcement height, and other engineering variables. Automesh automatically divides each bead into layers and each layer into passes according to aspect-ratio criteria and locally refines the mesh in regions prone to poor element quality, such as the root and HAZ. By seamlessly integrating Automesh for preprocessing with IEFEM for calculation, the present research achieves full automation from model creation to solution execution. Compared with conventional practices, overall throughput is accelerated by two to three orders of magnitude, and both mesh quality and labour requirements are simultaneously reduced. The resulting reduction in turnaround time

shortens the iterative loop of design, analysis and quality assurance, thereby lowering the lead time and cost of bringing welded products to market.

OUTLINE OF THE IDEALISED EXPLICIT FEM

The Idealised Explicit Finite-Element Method (IEFEM) reformulates the dynamic-explicit FEM so that quasi-static thermo-elastic-plastic welding problems can be solved with minimal run-time and memory while preserving implicit-level accuracy [5]. It executes large-scale multi-pass or assembly-welding simulations through the following cycle (Fig. 1):

I. Incremental equilibrium cycle
At every time step, the solver performs three operations:

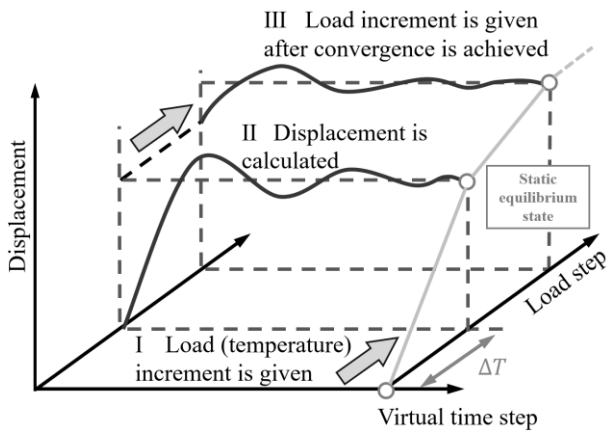

Fig. 1 Concept of Idealised Explicit FEM

- Load (temperature) increment is given: A new thermal or mechanical increment ΔT, ΔF is imposed and held constant.
- Displacement calculation: Nodal displacements are advanced using the explicit update.

$$\left(\frac{1}{\Delta t^2}[M]+\frac{1}{2\Delta t}[C]\right)\{U\}_{t+\Delta t}=\{F\}_t-\sum_{e=1}^{N_e}\int_{V^e}[B]^T\{\sigma\}dV$$
$$-\frac{2}{\Delta t^2}[M]\{U\}_t-\left(\frac{1}{\Delta t^2}[M]-\frac{1}{2\Delta t}[C]\right)\{U\}_{t-\Delta t} \quad (1)$$

where $[M]$, $[C]$, $[B]$ and $\{\sigma\}$ denote the mass, damping, strain-displacement and stress terms, respectively; $\{U\}$ and $\{F\}$ are the displacement and load vectors, N_e the number of elements, and V_e the volume of element e.

- Next increment after convergence: When equilibrium is achieved, the solver returns to step 1 for the next $\Delta T, \Delta F$.

II. Diagonal mass and damping: Instead of retaining full, coupled matrices, IEFEM lumps both the mass and damping terms such that each degree of freedom carries its own independent scalar mass and damping value. The mass assigned to each node is chosen so that a stress wave crosses any element in only a few explicit time steps, making the admissible time-step size almost uniform across the mesh regardless of element size or material. The damping for each node is then set to the "critical" value implied by its local mass and stiffness, which suppresses numerical oscillations as quickly as possible.

Because these diagonal (one-value-per-DOF) matrices do not create global couplings, the explicit update requires no linear-system solver, significantly reduces memory usage, and lets the analysis proceed with the largest stable time step. Consequently, the result is far fewer iterations before static equilibrium is reached and a substantial reduction in overall run-time.

III. Parallel-computing advantage: Because every update involves only element-local or DOF-local data, the method parallelises efficiently on GPUs: thousands of threads can integrate elements independently, delivering further speed-ups beyond the intrinsic efficiency gains of IEFEM.

THEORETICAL FRAMEWORK AND WORKFLOW OF AUTOMESH

Automesh builds on the Gmsh kernel [12], supplementing its geometry-independent mesher with welding-specific intelligence that converts engineering parameters directly into a finite-element analysis-ready model. The workflow begins by reading the joint descriptors - groove angle α, bevel depth, root gap g, number of layers n, number of passes m, target pass aspect ratio, and so on. A consistency check eliminates physically impossible combinations and normalises the parameter set.

The validated parameters are then cast into closed-form expressions that define the two-dimensional weld cross-section. For a V-groove, the upper width at height z is, for example:

$$W(z) = 2(z - z_0 - t_r)\tan\frac{\alpha}{2} + g \tag{2}$$

with z_0 the root reference level and t_r the root-face thickness. Using such relations, an optimisation routine subdivides the weld deposit into *n* layers and *m* passes whose thicknesses and widths balance filler-metal volume with heat-input distribution.

For every layer-pass pair, a boundary point cloud is generated, and a physically based envelope is added to represent the heat-affected zone (HAZ). At this stage, the algorithm also assigns region-dependent target element sizes: the weld bead and HAZ receive a finer characteristic length to resolve steep thermal gradients and stress concentrations, whereas the far-field base plate is allocated a coarser length to economise on degrees of freedom. This graded specification is read from a configuration file and propagated automatically through all subsequent meshing steps.

The two-dimensional entities are extruded or revolved to create the three-dimensional solid; axial and circumferential element counts are chosen such that the imposed aspect-ratio and regional size targets are simultaneously satisfied. The resulting volume is passed to Gmsh, which produces a tetrahedral mesh and evaluates each element with the quality measure

$$q(T) = \frac{4\sqrt{3}\cdot \mathrm{Area}(T)}{|e_1|^2+|e_2|^2+|e_3|^2} \tag{3}$$

Elements that fail the threshold trigger local refinement until the entire mesh meets the criterion. Because all geometric descriptions are analytic and the segmentation algorithm operates directly on the parameter set, the computational complexity is reduced from the $O(n^3 \log n)$ typical of conventional scripts to approximately $O(n \times m)$, where n and m are the layer and pass counts.

Finally, Automesh exports the geometry and mesh files together with quality statistics. In practical multi-pass joints, the fully automated pipeline reduces hours of manual modelling effort into a few seconds and delivers a graded mesh that concentrates resolution precisely where the welding physics demand it.

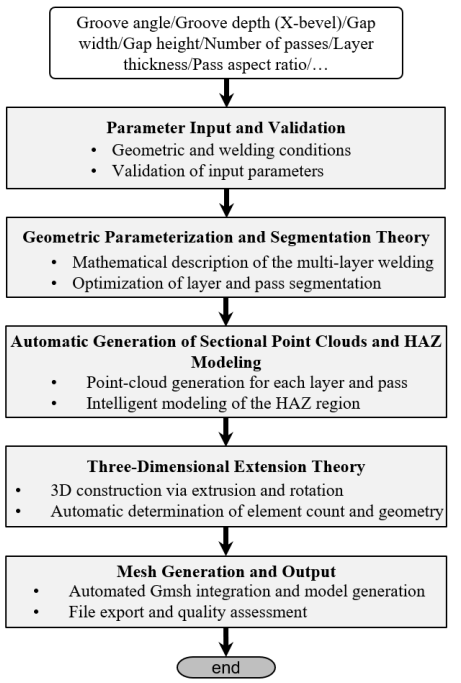

Fig. 2 Automesh workflow for parameter-based generation of graded finite-element meshes in multi-pass welding

LARGE-SCALE MULTI-PASS WELDING CASE STUDY USING AUTOMESH AND THE IDEALISED EXPLICIT FEM

This section demonstrates a large-scale multi-pass welding simulation that couples the Idealised Explicit FEM of Section 2 with the Automesh workflow of Section 3. To verify the approach, transverse shrinkage and angular distortion are evaluated while systematically varying key geometric parameters.

INFLUENCE OF GROOVE DEPTH ON TRANSVERSE SHRINKAGE AND ANGULAR DISTORTION

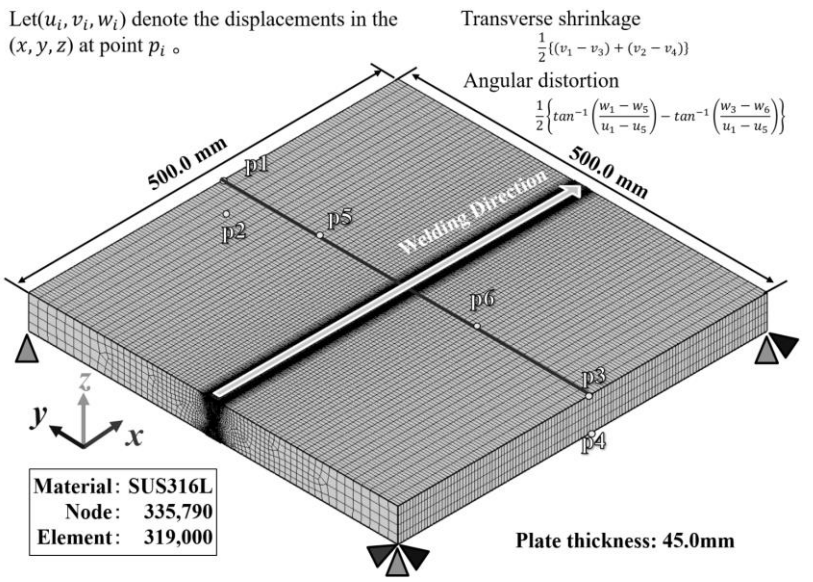

Fig. 3 Geometry and dimensions of the X-groove multi-layer welding model

Fig. 3 illustrates the model geometry: two SUS316L plates, 500 mm long, 250 mm wide and 45 mm thick, joined by an X-groove weld. Table 1 lists the constant process parameters used throughout - heat-input density q, welding speed v, root gap g, reinforcement height $h_{rein}$and groove angles α_{top} , α_{bottom}. The only variable parameter is the upper groove depth d_{upper}, which is reduced from 41 mm to 4 mm in twelve discrete steps. Fig. 4 shows the reference case in conjunction with comparative meshes for all groove-depth variants. In all simulations, welding proceeds sequentially from left to right, depositing the upper passes before the lower passes.

The reference model contains 335,790 nodes and 319,000 elements. Temperature-dependent material properties for SUS316L (Fig. 5) are employed. The moving heat source is represented by Goldak's double-ellipsoidal Gaussian distribution, and newly deposited passes are activated dynamically via the element-birth technique.

Fig. 6 presents the transient temperature distribution recorded during the 15th welding pass for the X-groove joint with a groove depth d_{upper} = 24 mm. The snapshot illustrates the operational profile of Goldak's heat source, while the absence of activated elements ahead of the melt front confirms that element-birth activation is functioning correctly.

Fig. 7 demonstrates the temporal evolution of deformation for the reference case, with transverse shrinkage in (a) and angular distortion in (b). The detailed resolution of deformation history highlights that IEFEM is capable of capturing not only the final distortion but also the intermediate accumulation process with both high accuracy and high computational efficiency. Most of the deformation occurs during the heating phase, while the subsequent cooling phase contributes only marginally, confirming that the method enables detailed, physics-based analysis rather than a simplified estimation of distortion.

Fig. 8 presents the peak-temperature contours during the final welding pass for six representative groove depths. In all cases, welding was carried out following an identical sequence - from top to bottom and left to right - such that the final pass was consistently located at the lower-right corner. This consistent sequencing minimizes the influence of pass-order variations and ensures comparability across all models.

The contours further reveal that the size of the molten region exceeding 1500 °C in the final pass varies with groove depth and shows a clear positive correlation with the cross-sectional area of the corresponding pass. This indicates that the Automesh system automatically adjusts the total heat input according to the pass cross-sectional area, thereby maintaining a constant heat-input density per unit area. As a result, the total heat input in each case depends solely on the deposited cross-sectional area and is independent of groove-depth differences. This mechanism effectively constrains the thermal boundary conditions, ensuring that the observed variations in transverse shrinkage and angular distortion arise only from geometric effects rather than inconsistencies in heat input.

The residual transverse stress distribution σ_{yy}, along the mid-width direction is shown in Fig. 9. Tensile peaks appear immediately adjacent to each weld bead, while a compressive trough develops near the plate centre. The location of maximum compressive stress shifts with groove depth, reflecting the interplay between tensile strains in the fusion zones and compressive contraction in the surrounding base metal.

The transverse shrinkage and angular distortion were evaluated on the mid-length cross-section of the plate; measurement directions are indicated at the top of Fig. 3. Fig. 10 presents the computed deformation results: in both sub-plots the abscissa corresponds to the pass number, whereas the ordinate represents transverse shrinkage in (a) and angular distortion

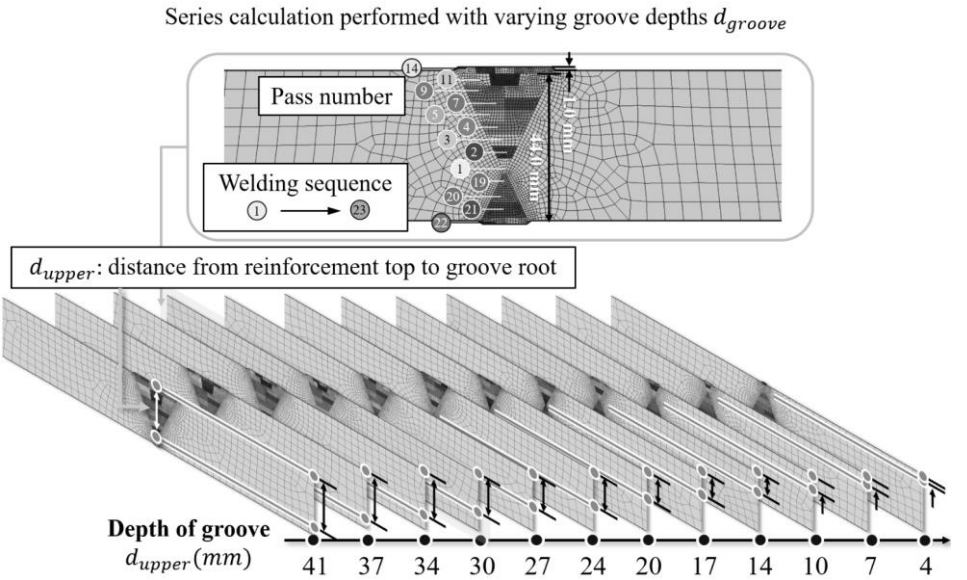

Fig. 4 Cross-sectional mesh layout and pass sequence, with comparative meshes for the twelve groove-depth cases (d_{upper})

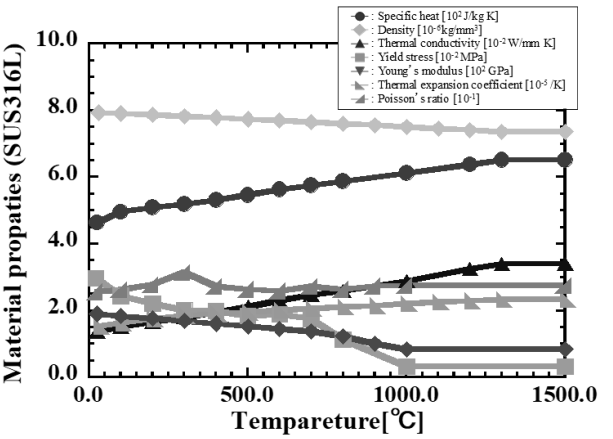

Fig. 5 Temperature-dependent material properties of SUS316L adopted in the analysis

Table 1 Geometric dimensions of the model and welding process parameters used in the simulations

Parameter	Symbol (unit)	Value
Heat-input density per unit area	$q(W/mm^2)$	50.0
Welding speed	$v(mm/s)$	3.0
Root gap	$g(mm)$	1.0
Reinforcement height	$h_{rein}(mm)$	1.0
Groove angle (top side)	$\alpha_{top}(deg)$	50
Groove angle (bottom side)	$\alpha_{bottom}(deg)$	50
Aspect ratio of passes per layer	—	≈ 1 : 3

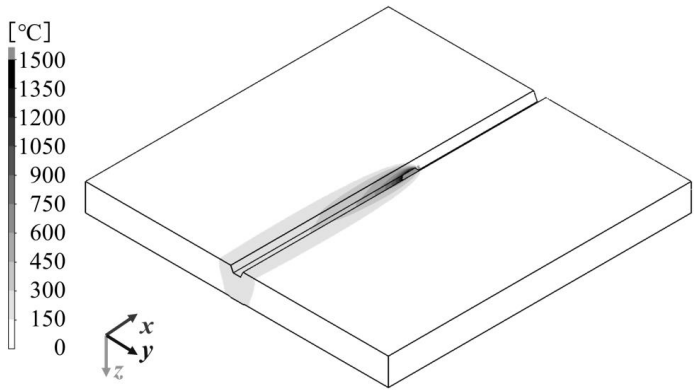

Fig. 6 Transient temperature distribution recorded during the 15th welding pass for the X-groove joint with the groove depth d_{upper} at 24 mm

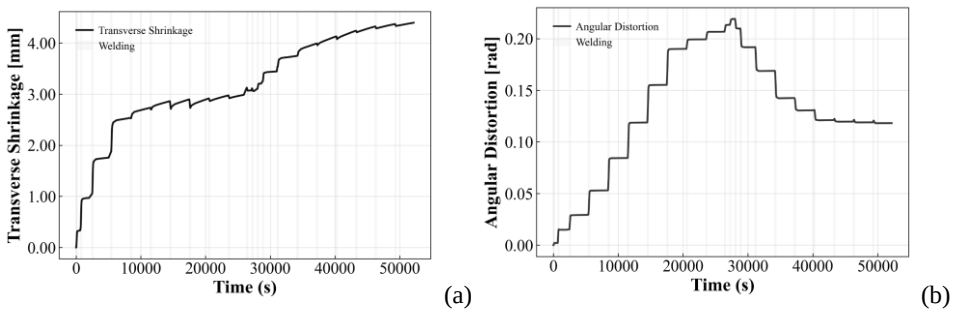

Fig. 7 Transient deformation history captured of the X-groove joint with a groove depth d_{upper} at 24 mm. (a) transverse shrinkage; (b) angular distortion

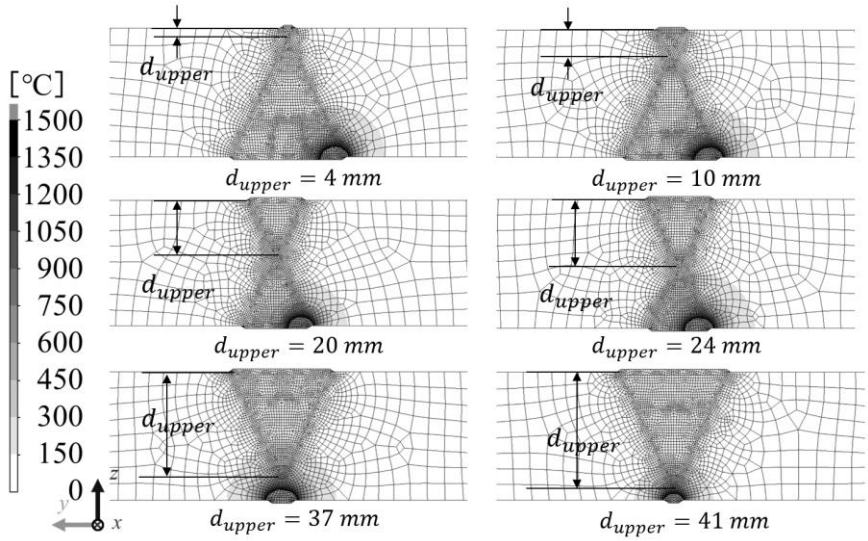

Fig. 8 Peak-temperature distribution during the final welding pass for X-groove multi-layer joints with varying groove depths d_{groove}

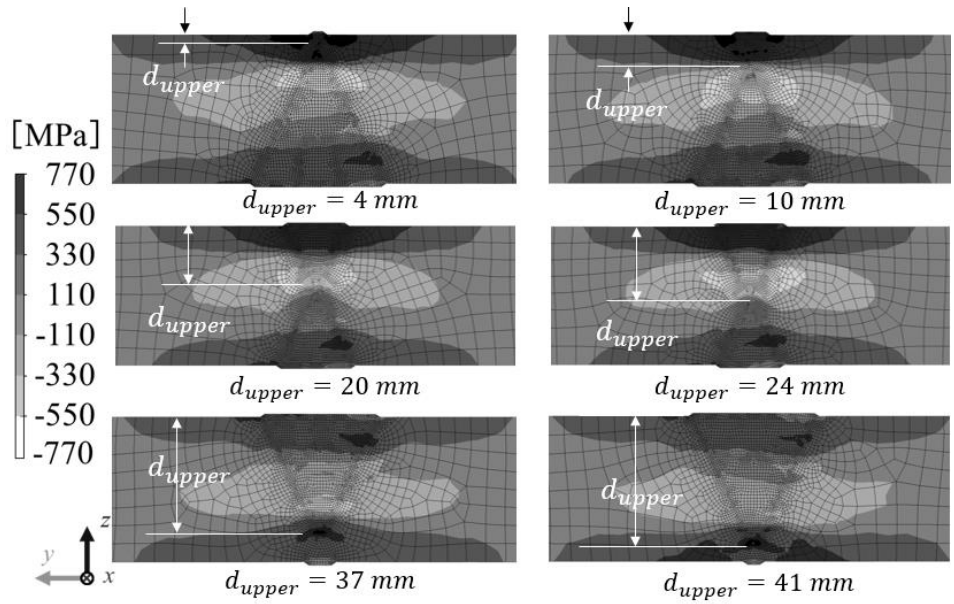

Fig. 9 Transverse residual-stress distribution (along the plate-width y direction) at the mid-length cross-section during the final welding pass for X-groove multi-layer joints with different groove depths $d$groove d_{groove}

in (b). Across the twelve groove-depth cases, the intermediate depth around 24 mm exhibits the smallest shrinkage and distortion, while both the shallowest groove (4 mm) and the deepest groove (41 mm) cases show noticeably larger deformations.

The results suggest that when the upper and lower V-grooves are of comparable size (i.e., the X-groove is approximately symmetric through the thickness), the thermal loading and the associated shrinkage-induced bending moments about the plate mid-surface tend to counterbalance, thereby suppressing overall twist and rotation. Conversely, when the groove geometry becomes markedly asymmetric (a small V opposite a large V), the imbalance of through-thickness bending moments leads to greater an··gular distortion. This trend highlights the strong influence of groove symmetry on the distortion response. Future investigations that incorporate a quantitative evaluation of section resultants - via integration of the through-thickness shrinkage/inherent strain field - or direct comparison with double-sided deposition on a symmetric cross-section could provide deeper mechanistic validation of this interpretation.

For each of the twelve groove-depth cases, Automesh produced the three-dimensional mesh in about 10 secs from parameter input. Replicating the same unit-pass heat input and element quality manually with commercial CAD/CAE software would require at least 30 h even for an experienced analyst. The thermo-elastic-plastic analysis of the 27-pass model (319,000 elements) finished in 8 h 21 min on a single RTX2080 Ti using the Idealized Explicit FEM - approximately one-tenth of the runtime reported for an implicit commercial solver. When the twelve groove-depth cases were distributed across twelve GPUs, the entire pipeline - from preprocessing to results - was completed in less than half a day, underscoring the dramatic improvement in efficiency and throughput achieved by the Automesh in combination with IEFEM workflow.

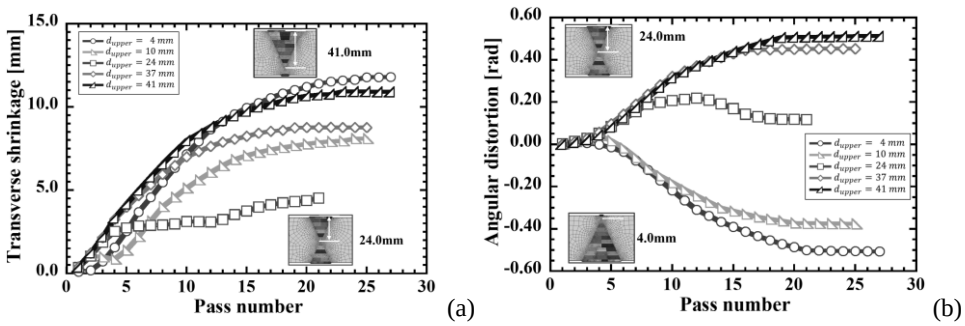

Fig. 10 Deformation trends with increasing pass number for the twelve groove-depth cases(a)Relationship between transverse shrinkage and pass number(b) Relationship between angular distortion and pass number

INFLUENCE OF GROOVE ANGLE ON ANGULAR DISTORTION

Fig. 11 depicts the second test configuration: two carbon-steel plates 500 mm × 250 mm × 45 mm are joined by a V-groove weld whose included angle α is the only variable. The unit heat-input density q, welding speed v, root gap g and reinforcement height h_{rein} are kept identical to those in Table 1, while α is varied from 40° to 70° in 5° increments, yielding seven cases. The upper part of Fig. 12 gives the pass layout and weld sequence for the 70° joint; the lower part juxtaposes the cross-sectional meshes for all groove angles. As in the previous section, welding proceeds from the left edge to the right, depositing all upper passes first and all lower passes afterwards. Because a smaller α narrows the groove opening, the number of passes required to preserve the target aspect ratio decreases, and the final model size converges to roughly one million elements for the 45-pass case.

Fig. 13 shows the transverse residual-stress distributions σ_{yy} along the plate-width (y) direction for three representative V-groove cases ($\alpha = 40°, 55°, 70°$) out of the seven analysed. It is evident that as the groove angle increases, the spatial extent of both tensile and compressive stresses widens. Consistent with the X-groove results of the previous section, compressive peaks remain concentrated at the groove root, while tensile stresses dominate near the plate surfaces on either side of the weld.

Fig. 14 summarises the angular-distortion results. (a) traces the cumulative angular distortion against pass number, and (b) relates the angular distortion to pass height (through-thickness position). With element-birth activation and residual stresses fully accounted for, a smaller groove angle not only shortens the pass sequence but also reduces the overall angular distortion. Under the present setting of constant unit heat-input density q and welding speed v, narrowing the groove decreases the deposited cross-sectional area and the number of passes required; consequently, the accumulated heat input per unit length of joint is reduced. The lower energy input leads to smaller thermal expansion and plastic flow in the fusion and HAZ regions and, therefore, to a uniformly smaller incremental contribution to angular distortion at a given height (see Fig. 14b). Accordingly, the widest groove ($\alpha = 70°$) - which requires 45 passes and yields the largest mesh - accumulates the greatest net lineal heat input and exhibits the largest angular distortion, whereas the narrowest groove ($\alpha = 40°$) shows the least. While this energy-based interpretation is qualitative, it is consistent with the observed monotonic decrease in angular distortion as α decreases.

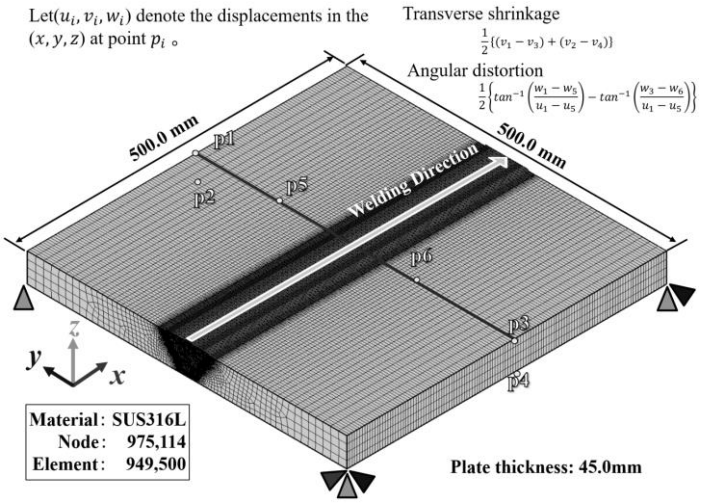

Fig. 11 Geometry and dimensions of the V-groove multi-layer welding model

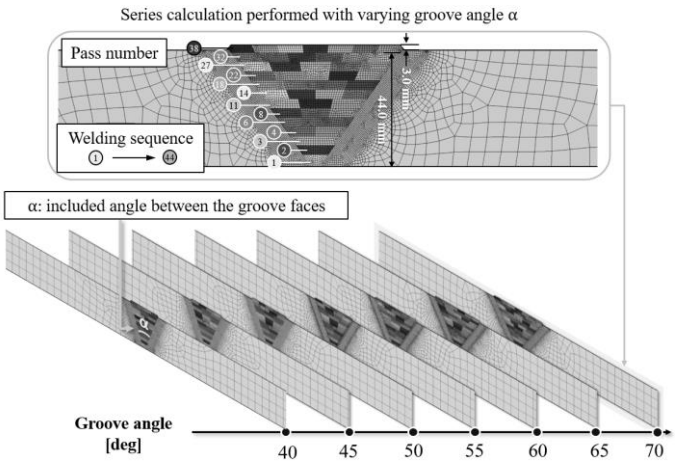

Fig. 12 Cross-sectional meshes for the seven groove-angle cases (40°-70°) and pass layout for the 70° reference joint

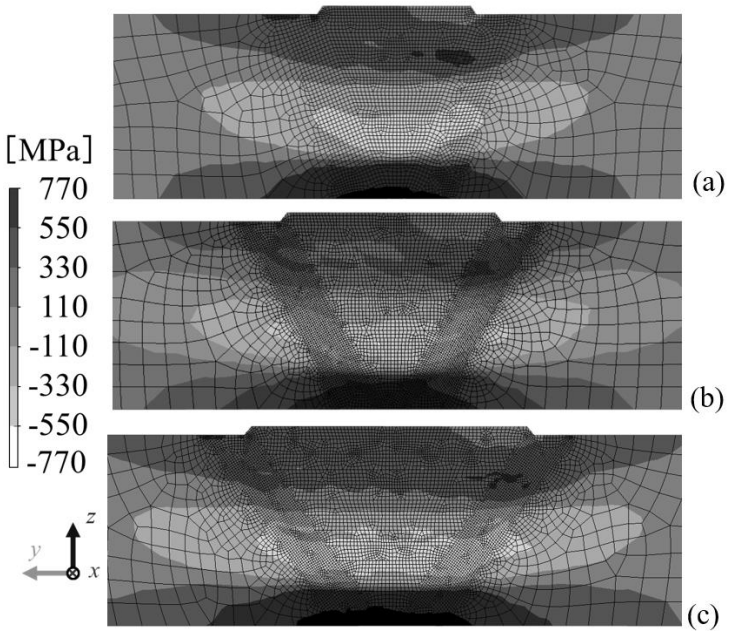

Fig. 13 Transverse residual-stress distribution (along the plate-width *y* direction) at the mid-length cross-section during the final welding pass for V-groove multi-layer joints with different groove angles α : (a) 40°; (b) 55°; (c) 70°

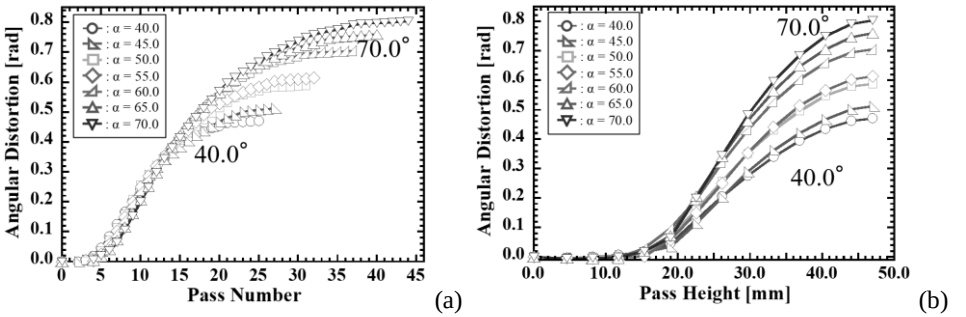

Fig. 14 Angular distortion for the seven groove-angle cases(a) variation with pass number(b) variation with pass height

INFLUENCE OF SIMULTANEOUS VARIATIONS IN GROOVE ANGLE AND ROOT GAP: A LARGE-SCALE MULTIVARIATE STUDY WITH AUTOMESH

To assess the industrial versatility of the proposed workflow, a two-parameter investigation was performed on the V-groove joint introduced in the previous section. Both the groove angle α and the root gap g were treated as independent variables, whereas all other geometric and process conditions correspond to those in Table 2. As illustrated in Fig. 15, α and g were independently sampled within the intervals $\alpha \in [40^{\circ}, 70^{\circ}]$ and $g \in [1\,mm,\ 10mm]$, respectively, producing 110 distinct cases. For every case Automesh generated a three-dimensional mesh in approximately 10 s, after which the Idealised Explicit FEM solved the thermo-elastic-plastic problem. The resulting parametric study is of a scale that would be essentially unattainable with manual CAD/CAE workflows.

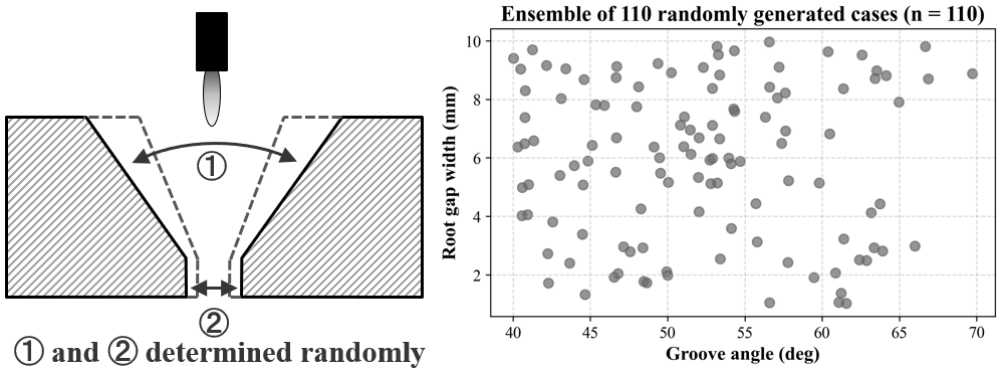

Fig. 15 Schematic illustration of the V-groove cross-sectional variables and the sampling ranges used in the study

Table 2 Numerical settings and descriptions of the variable and fixed parameters adopted for the multivariate analysis

Category	Parameter	Value / Range	Description
Variable Parameters	①Groove angle	40.0° - 70.0°	Randomly sampled within this range
	②Root gap	1.0 mm - 10.0 mm	Randomly sampled within this range
Fixed Parameters	Root gap height	1.0 mm	Constant across all configurations
	Layer thickness	First: 4.67 mm Intermediate: 3.67mm Final: 3.00 mm	Fixed by layer type
	Number of passes	Closest to aspect ratio 1:3	Determined to approximate the aspect ratio
	Heat input	50.0 $\mathrm{J/mm^2}$ (proportional to cross-sectional area)	Uniform per pass
	Welding speed	3.0 mm/s (all passes)	Constant across all passes

Fig. 16 presents the three-dimensional results, where the abscissae are given by α and g, and the ordinates represent (a) transverse shrinkage and (b) angular distortion. The two planes correspond to least-squares regression surfaces fitted to all data points. To isolate individual effects, Fig. 17 plots deformation as a function of root gap alone. No clear correlation is observed for either transverse shrinkage or angular distortion, indicating that within the examined range, root gap is not a dominant factor governing global deformation.

In contrast, Fig. 18 reveals a different trend: when examining the groove angle, both transverse shrinkage and angular distortion increase monotonically with α, with the latter exhibiting two abrupt "jumps." The corresponding groove angles and pass distributions are indicated in the inset diagrams.

To clarify the underlying mechanism, Fig. 19 re-expresses the data in terms of the relationship between the heat input of individual passes and the incremental contributions to transverse shrinkage and angular distortion. The horizontal axis denotes the heat-input parameter, $Q/h_{\max}^2$, while the vertical axes represent (a) the transverse-shrinkage increment and (b) the angular-distortion increment. Here, $h_{\max}$ is defined as the distance from the upper end of each pass to the bottom edge of the base plate. This choice of $h_{\max}$ reflects the fact that transverse shrinkage and angular distortion are evaluated with respect to the plate bottom surface; by treating each pass as equivalent to a bead-on-plate weld located at its corresponding height, $h_{\max}$ serves as a mechanical lever arm that rationally captures the positional dependence of deformation.

The intermediate polynomial fits, determined by the least-squares method, reveal a nonlinear correlation between the heat-input parameter $Q/h_{\max}^2$ and the deformation increments. This trend is consistent with the well-established functional relationship reported in bead-on-plate welding studies, where both transverse shrinkage and angular distortion scale

nonlinearly with Q/h^2 [19]. The similarity between the present multi-pass results and classical bead-on-plate data indicates that the empirical framework developed for single-pass welding remains applicable to predicting dominant directional deformations in multi-pass welds. Minor discrepancies between the fitted curves and individual data points are attributable to geometric effects such as the root gap and numerical interpolation procedures; nevertheless, the overall distribution confirms that the bead-on-plate analogy provides a robust physical interpretation for the observed deformation behaviour.

Fig. 20 compares cross-sections immediately before and after the distortion jumps. As illustrated, during the monotonic increase of groove angle, the difference between cases 2 and 3 as well as between cases 5 and 6, is simply that the pass layer marked by the yellow box changes from a single pass to two passes. To ensure equivalent total heat input, the heat input per unit pass area is preserved, meaning that when one pass is split into two, the heat-input parameter $Q/h_{\max}^2$ is equally divided. However, as shown in Fig. 19, angular distortion reaches a local maximum around $Q/h_{\max}^2 \approx 5$. Under this condition, splitting the heat input between two passes instead of one markedly amplifies angular distortion.

Fig. 21 quantifies the consequence of this mechanism. In the critical layer, angular distortion increases from 0.007 rad in the single-pass case (case 5) to a combined 0.035 rad (0.015 + 0.020 rad) in the two-pass case (case 6). This sudden jump arises because splitting the pass redistributes the same heat input into two passes, each with a slightly smaller Q, but both still located at small $h_{\max}$. As a result, their $Q/h_{\max}^2$ values remain in the peak region of the distortion–parameter curve (see Fig. 19), producing two relatively large distortion increments instead of one moderate increment. In contrast, when pass subdivision occurs at larger groove angles, the affected passes are located at greater $h_{\max}$, where $Q/h_{\max}^2$ is much smaller and lies within the nearly proportional region of the curve. In this regime, further subdivision reduces distortion smoothly, and no discrete change is observed.

For transverse shrinkage, the trend differs. As shown in Fig. 21(a), the fluctuation is modest - from 1.34 mm to 2.16 mm - compared with the overall shrinkage of approximately 15 mm. This is because transverse shrinkage depends mainly on the integrated contraction volume across the joint width, which varies smoothly with groove geometry. Unlike angular distortion, it does not couple strongly with the through-thickness lever arm represented by $h_{\max}$; thus, even under the same subdivision conditions highlighted in Fig. 20, shrinkage remains continuous without abrupt jumps.

The discrete geometric effects identified here could only be captured because Automesh enforced identical element quality and pass placement across all 110 simulation cases, eliminating meshing bias and ensuring that differences in deformation arose solely from groove geometry. Furthermore, the Idealised Explicit FEM, executed on eight RTX 2080 Ti GPUs, solved all thermo-elastic-plastic models within approximately two weeks - an undertaking that would be prohibitively time-consuming with conventional implicit solvers. This computational efficiency renders the workflow practical for large-scale design-space explorations and enables the generation of high-fidelity datasets well suited for machine-learning applications.

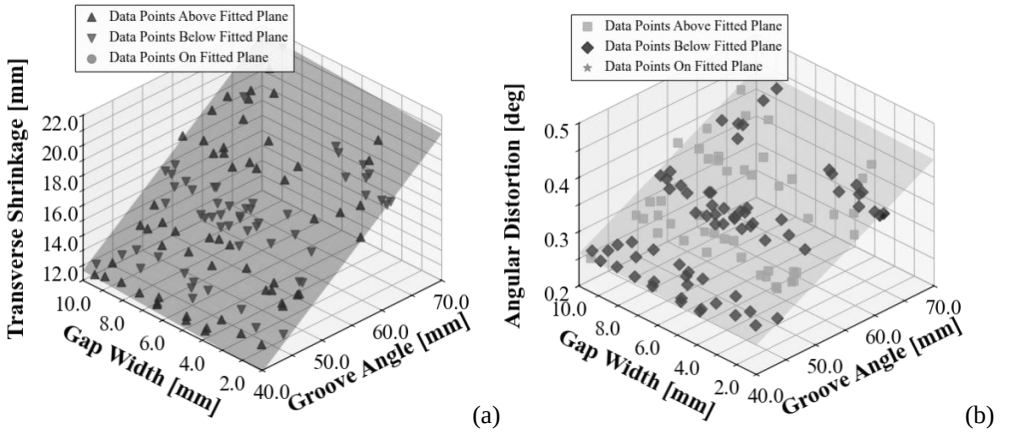

Fig. 16 Influence of groove angle and root gap on weld-induced deformation in V-groove multi-pass joints(a) Transverse shrinkage plotted against groove angle α and root gap g(b) Angular distortion plotted against groove angleαand root gap g

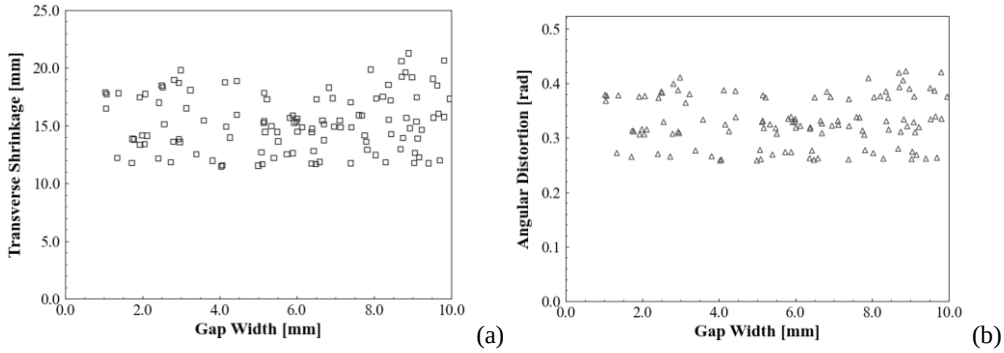

Fig. 17 Influence of root gap on deformation responses in V-groove multi-pass welding (a) Transverse shrinkage versus root gap g (b) Angular distortion versus root gap g

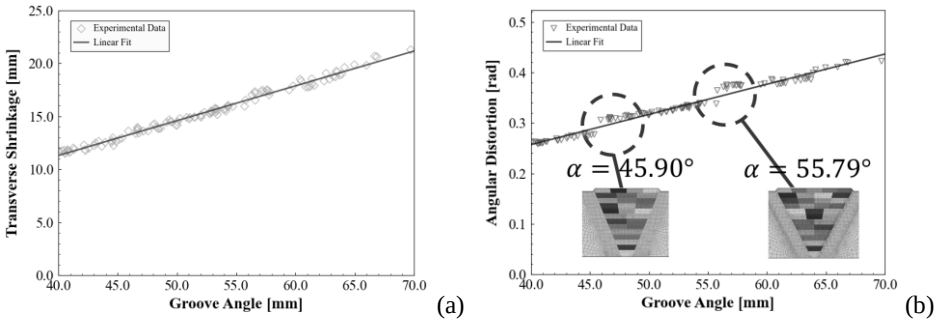

Fig. 18 Influence of groove angle on deformation responses in V-groove multi-pass welding(a) Transverse shrinkage versus groove angle α (b) Angular distortion versus groove angle α

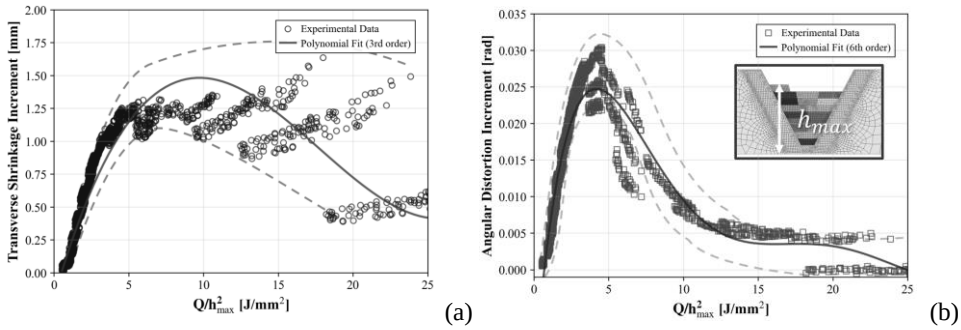

Fig. 19 Deformation increment analysis: correlation between maximum heat input parameter and weld distortion components(a) Transverse shrinkage increment vs $Q/h^2_{\max}$ (b) Angular distortion increment vs $Q/h^2_{\max}$

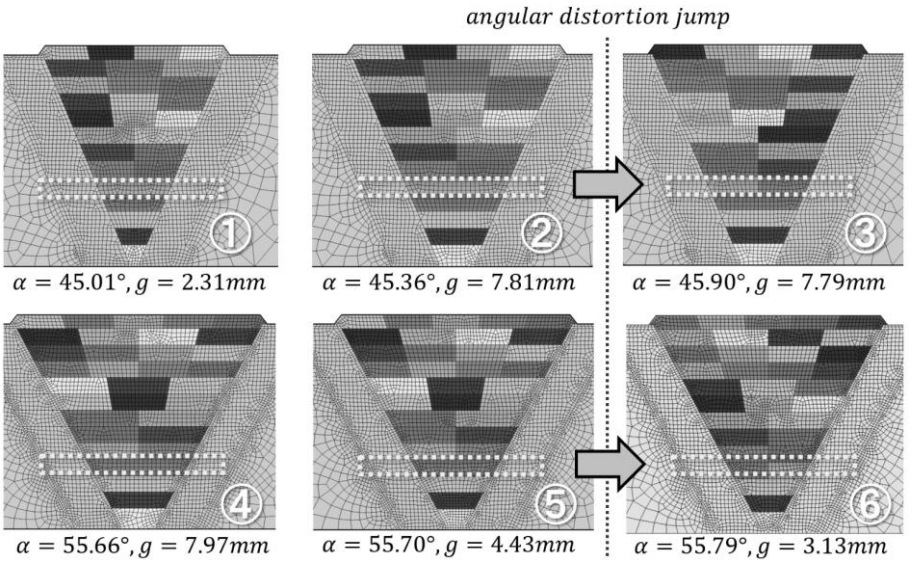

Fig. 20 Cross-sectional views immediately below and above the critical groove-angle threshold, showing how a discrete change in the number of passes within the dominant height band (shaded) amplifies the resulting angular distortion

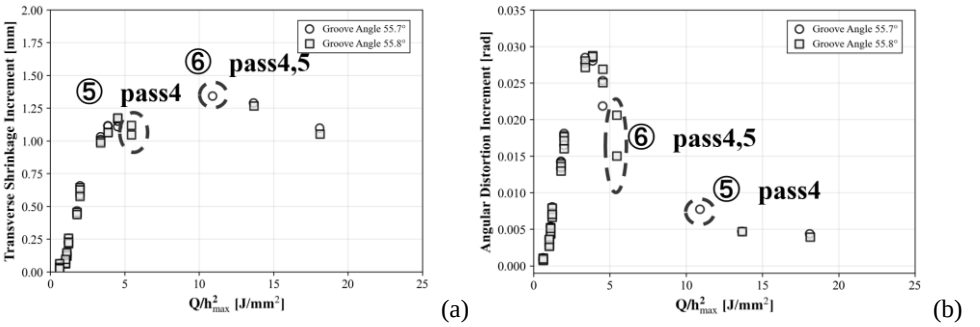

Fig. 21 Comparative analysis of weld deformation increments across different groove configurations (a) Transverse shrinkage increment vs $Q/h_{\max}^2$ (b) Angular distortion increment vs $Q/h_{\max}^2$

CONCLUSIONS

This study integrated the parameter-driven meshing tool Automesh with the memory-efficient, GPU-accelerated Idealised Explicit FEM (IEFEM) and applied the workflow to ultra-large, multi-pass weld joints. Across all cases, the framework delivered accuracy comparable to static implicit analyses while substantially improving computational efficiency, enabling practical, high-fidelity parametric studies. The main conclusions within the investigated configurations and parameter ranges are as follows:

1. The workflow performs thermo-elastic–plastic analyses across multiple multi-pass welding models, producing detailed, pass-resolved transient temperature, stress, and strain fields rather than only final deformation metrics.
2. Automesh enforced equal unit heat-input density per pass and consistent element quality / pass placement across all models, suppressing meshing bias and ensuring that inter-case differences stem from geometry rather than discretisation or heat-input inconsistency.
3. For X-groove joints, a groove depth close to one-half of the plate thickness (upper and lower V's comparable) produced the smallest transverse shrinkage and angular distortion, whereas shallower or deeper depths led to larger deformations. A through-thickness thermal-moment balance at the near-symmetric depth is a plausible explanation (qualitative).
4. For V-groove joints with constant unit heat-input density and welding speed, decreasing the groove angle α reduced the deposited cross-section and the number of passes, lowering the accumulated lineal heat input; over $\alpha = 40^\circ - 70^\circ$, both shrinkage and angular distortion increased monotonically with α. Within $g = 1 - 10$ mm, root gap showed no clear correlation with global deformation.
5. The residual-stress pattern was robust across cases: compressive peaks concentrated near the groove/root region, while tensile stresses dominated near the plate surfaces adjacent to the weld; the spatial extent of these zones broadened as α increased.
6. Two discrete jumps in angular distortion were traced to a change in pass count within a dominant height band. When a single pass is split into two under equal unit heat-input density, both sub-passes can fall closer to the peak of the empirical $Q/h_{\max}^2$–response curve, amplifying rotation and altering the local bending-moment distribution.
7. The study encompassed 110 V-groove models, each mesh containing hundreds of thousands up to $\sim 10^6$ elements. Automesh reduced mesh preparation to ~ 10 s per case; executed on eight RTX 2080 Ti GPUs, IEFEM produced fully converged thermo-elastic–plastic solutions for all models in ~ 2 weeks of wall-clock time - performance that makes large design-space exploration and machine-learning–ready datasets feasible for multi-pass welding.

References

[1] J. A. GOLDAK and M. AKHLAGHI**:** *Computational Welding Mechanics*, Springer, New York, 2005.

[2] L.-E. LINDGREN: 'Finite element modelling and simulation of welding–Part 1: Increased complexity', *Journal of Thermal Stresses*, 24 (2001), 795-837.

[3] C. DENG and M. MURAKAWA: 'Numerical simulation of temperature field and residual stress in multi-pass welding of SUS304 pipe', *Computational Materials Science*, 37 (2006), 269-277.

[4] M. SHIBAHARA, K.IKUSHIMA, S. ITOH and K. MASAOKA: 'Computational Method for Transient Welding Deformation and Stress for Large Scale Structure Based on Dynamic Explicit FEM', *Quarterly Journal of the Japan Welding Society*, Vol.29, No.1(2011), pp.1-9. (Japanese/English).

[5] P. WRIGGERS: *Nonlinear Finite Element Methods*, Springer (2008), pp.209-212.

[6] T. HARADA, S. KOSHIZUKA and Y. KAWAGUCHI: 'Smoothed particle hydrodynamics on gpus', *Proceedings of Computer Graphics International*, Budmerice, Slovakia (2007), pp.63-70.

[7] A. KOLB, L. LATTA and C. REZK-SALAMA: 'Hardware based simulation and collision detection for large particle systems', Proceedings of the *ACM SIGGRAPH/EUROGRAPHICS Conference* on Graphics Hardware, Grenoble, France (2004), pp.123-131.

[8] Y. LIU, X. LIU and E. WU: 'Real-time 3d fluid simulation on gpu with complex obstacles, Proceedings of Computer Graphics and Applications', *Proceedings of the 12th Pacific Conference on Computer Graphics and Applications (PG'04)*, Seoul, Korea (2004), pp.247-256.

[9] K. IKUSHIMA, S. ITOH and M. SHIBAHARA: Development of Parallelized Idealized Explicit FEM Using GPU, *Quarterly Journal of the Japan Welding Society*, Vol.31, No.1 (2013), pp.23-32.

[10] J. R. SHEWCHUK: 'Triangle: Engineering a 2-D Quality Mesh Generator and Delaunay Triangulator'. In *Applied Computational Geometry: Towards Geometric Engineering* (M. C. Lin & D. Manocha, eds.), Lecture Notes in Computer Science, Vol. 1148, Springer, Berlin, 1996, pp. 203-222.

[11] H. SI: 'TetGen, a Delaunay-Based Quality Tetrahedral Mesh Generator', *ACM Transactions on Mathematical Software*, 41 (2) (2015), Article 11, 11:1-11:36.

[12] C. GEUZAINE and J.-F. REMACLE: 'Gmsh: A 3-D Finite Element Mesh Generator with Built-in Pre- and Post-Processing Facilities', *International Journal for Numerical Methods in Engineering*, 79 (11) (2009), 1309-1331.

[13] CGAL PROJECT: 'CGAL 6.0 Release Notes', CGAL, September 2024. (online; accessed 28 July 2025).

[14] L.-E. LINDGREN: 'Finite Element Modelling and Simulation of Welding—Part 1: Increased Complexity'. *Journal of Thermal Stresses*, 24 (2) (2001), 141-192.

[15] K. IKUSHIMA, S. ITOH and M. SHIBAHARA: 'Development of Idealized Explicit FEM Using GPU Parallelization and Its Application to Large-Scale Analysis of Residual Stress of Multi-Pass Welded Pipe Joint', *Welding in the World*, 59 (4) (2015), 589-595.

[16] C. S. PATHAK, L. G. NAVALE, A. D. SAHASRABUDHE and M. J. RATHOD: 'Analysis of Thermal Cycle during Multipass Arc Welding', *Welding Journal*, 91 (5) (2012), 149-154.

[17] H. HUANG and H. MURAKAWA: 'Selective Integration-Based Adaptive Mesh Refinement for Accurate and Efficient Welding Process Simulation', *Journal of Manufacturing and Materials Processing*, 7 (6) (2023), 206.

[18] R. HU, S. PANG, X. CHEN, L. LIANG and T. HU: 'An Octree-Based Adaptive Mesh Refinement Method for Three-Dimensional Modelling of Keyhole-Mode Laser Welding', *International Journal of Heat and Mass Transfer*, 115 (2017), 258-263.

[19] K. SATOH and T. TERASAKI: 'Effect of welding condition on welding deformation in welded structural materials', *Journal of the Japan Welding Society*, 45 (1976), 302-308.